PNAS RESEARCH ARTICLE | ENGINEERING

Synthesizing ordered polar patterns in nonpolar $SrTiO_3$ nanofilms via wrinkle-induced flexoelectricity

Hongxing Shang[a,1], Tang Sheng[a,1], Huiting Dong[a,1], Yihan Wu[a,b], Qianqian Ma[a], Xin Zhang[a], Lingtong Lv[a], Hongyu Cao[a], Feng Deng[a], Xu Liang[a,2], Shuling Hu[a], and Shengping Shen[a,2]

Affiliations are included on p. 7.

Edited by Yonggang Huang, Northwestern University–Evanston, Glencoe, IL; received July 19, 2024; accepted October 29, 2024

Ordered polar structures in oxide nanofilms play a pivotal role in the development of nanoelectronic applications. Hitherto, ordered polar structures have been restricted to a limited number of ferroelectric materials, and there is no effective scheme to induce and manipulate ordered polar patterns in centrosymmetric nonpolar nanofilms due to the absence of spontaneous symmetry breaking. Here, we circumvent these limitations by utilizing the wrinkle-induced strain gradient modulation associated with flexoelectricity as a general means of inducing and manipulating ordered polar patterns in nonpolar nanofilms. Leveraging the surface instability caused by strain mismatch between oxide nanofilms and pre-strained compliant substrate, we successfully fabricate striped $SrTiO_3$ wrinkles, where well-ordered strain gradients and corresponding periodic polar patterns are readily achieved. Through in-situ piezoresponse force microscopy experiments, we show that the generated polar patterns can be manipulated by varying strain boundaries. Furthermore, the atomistic resolution images and first-principles calculations reveal that such wrinkle-induced ordered polar patterns primarily emerge from the flexoelectric coupling between the local polarization and strain gradients. These findings provide implications for manipulating polar structures by strain gradient and flexoelectric engineering, which in turn enable the realization of nontrivial polar structures in a broader range of materials.

flexoelectricity | nonpolar nanofilms | polar pattern | wrinkle

Ordered polar structures including polar stripes (1), mazes (2), merons (3), skyrmions (4–6), and vortices (7) in oxide films are of great importance considering their rich physical properties and prospective post-Moore applications in high-density nanoelectronic. However, the effective means to induce and manipulate ordered polar structures in centrosymmetric nonpolar materials has remained elusive owing to the absence of spontaneous symmetry breaking, which in turn restricts the practical applications of these ordered polar structures. This triggers the interest and demand of exploring a general strategy for inducing and manipulating ordered polar structures in a nonpolar material. Here, by recognizing the crucial role of the wrinkle-induced strain gradient associated with flexoelectricity, we theoretically and experimentally demonstrate the formation and manipulation of ordered polar patterns in wrinkled nonpolar nanofilms using a combination of piezoresponse force microscopy (PFM) scanning, aberration-corrected high-angle annular dark field (HAADF) atomic resolution imaging, and ab initio (first-principles) calculations. Our findings provide a universal flexoelectric strategy to fabricate and manipulate ordered polar patterns in nonpolar material systems, which is no longer restricted by ferroelectricity or superlattice structures.

Up to now, the nontrivial polar structures are more readily accessible in ferroelectric structures (7–11) [e.g. prototypical $PbTiO_3$ (PTO)/$SrTiO_3$ (STO) superlattice]. Although the STO/PTO superlattice is known to elicit polar antivortex in STO (12), it still relies on the electrostatic modulation by the pairing vortex in the ferroelectric PTO. Moreover, such ferroelectricity modulated by strains is invalid in centrosymmetric crystallographic point groups and generally suffers from its problematic size dependence (13, 14). We turn our attention to the strain gradient modulation and corresponding flexoelectricity in the wrinkled single-crystal STO nanofilm, which is known as a typical centrosymmetric nonpolar crystal without ferroelectric interference at room temperature. In contrast to ferroelectricity, this flexoelectricity (15–17) that describes the formation of electric polarization in the presence of nonuniform strains (strain gradients) is ubiquitous in all 32 crystalline point groups regardless of the crystal symmetry. Moreover, flexoelectricity benefits from the size reduction (18–20) and plays a quite significant or even dominant role in the polar transition of van der Waals materials (21) or nanofilms (22), where large strain

Significance

Ordered polar patterns hold intriguing physical properties and immense potential in nanoelectronic and electromechanical applications. However, the current ordered polar patterns observed in ferroelectrics are invalid for centrosymmetric nonpolar materials. How to effectively create and manipulate ordered polar structures in nonpolar nanofilms is still elusive. This study utilized the wrinkle-induced strain gradient modulation associated with flexoelectricity to provide a mechanical route to achieve ordered polar patterns in nonpolar nanofilms. Benefiting from such wrinkle-induced flexoelectricity, we extend the ordered polar structures from ferroelectric materials to a broader system of nonpolar materials, which in turn facilitate the development of high-performance nanoelectronic applications.

Author contributions: H.S., Q.M., L.L., F.D., X.L., S.H., and S.S. designed research; H.S., T.S., H.D., Q.M., and X.L. performed research; H.S., T.S., H.D., Y.W., and H.C. contributed new reagents/analytic tools; H.S., X.Z., and S.S. analyzed data; and H.S., X.L., and S.S. wrote the paper.

The authors declare no competing interest.

This article is a PNAS Direct Submission.

[1]H.S., T.S., and H.D. contributed equally to this work.

[2]To whom correspondence may be addressed. Email: xliang226@xjtu.edu.cn or sshen@mail.xjtu.edu.cn.

This article contains supporting information online at https://www.pnas.org/lookup/suppl/doi:10.1073/pnas.2414500121/-/DCSupplemental.

Published November 26, 2024.

gradients (up to $10^{6\sim7}$ m^{-1}) and pronounced flexoelectricity are easier to achieve. Thus, flexoelectricity should be a viable driving force to assign polarity and even ordered polar structures to centrosymmetric nonpolar nanofilms (23–26) if appropriate strain gradients can be introduced.

In this work, we employ surface wrinkling, a controllable instability phenomenon (27–30), to controllably introduce periodic strain gradients and engineer ordered polar patterns in STO nanofilms. Such surface wrinkling provides a fertile ground for generating strain gradients owing to its abundant local bending deformation (22). However, it is challenging to fabricate large-area wrinkles of nonpolar nanofilms due to their intrinsic brittleness. This might be the reason why, although recent theoretical predictions (31, 32) suggest the possibility of wrinkle-induced polar structures, the behavior and even existence of ordered polar patterns by wrinkling of nonpolar nanofilms have yet to be experimentally validated. By reducing the thickness of single-crystal STO membranes to less than 15 nm, we successfully fabricated large-area STO wrinkles utilizing the surface instability caused by strain mismatch between oxide nanofilms and pre-strained compliant substrate (33). Well-ordered polar patterns were subsequently observed within these wrinkled regions of STO nanofilms.

Results and Discussion

Structural Analysis. We epitaxially synthesized room-temperature paraelectric 15 nm STO films (Fig. 1*A*) to exclude the piezoelectric and ferroelectric interference. To trigger the surface wrinkling, we transferred the STO nanofilms onto a pre-stretched flexible polydimethylsiloxane (PDMS) substrate using the recently developed film growth and lift-off techniques (Fig. 1*B*) based on the water-soluble $Sr_3Al_2O_6$ (SAO) sacrificial buffer layer (34, 35) (*Materials and Methods*). After the transfer process, a compressive strain was imposed on the STO/PDMS system by releasing the pre-stretch strain. As a result, the STO/PDMS system spontaneously formed a wrinkled morphology owing to the modulus mismatch between the stiff oxide film and the compliant substrate (Fig. 1*C*). We examined the morphologies (Fig. 1*D*) and crystal structures

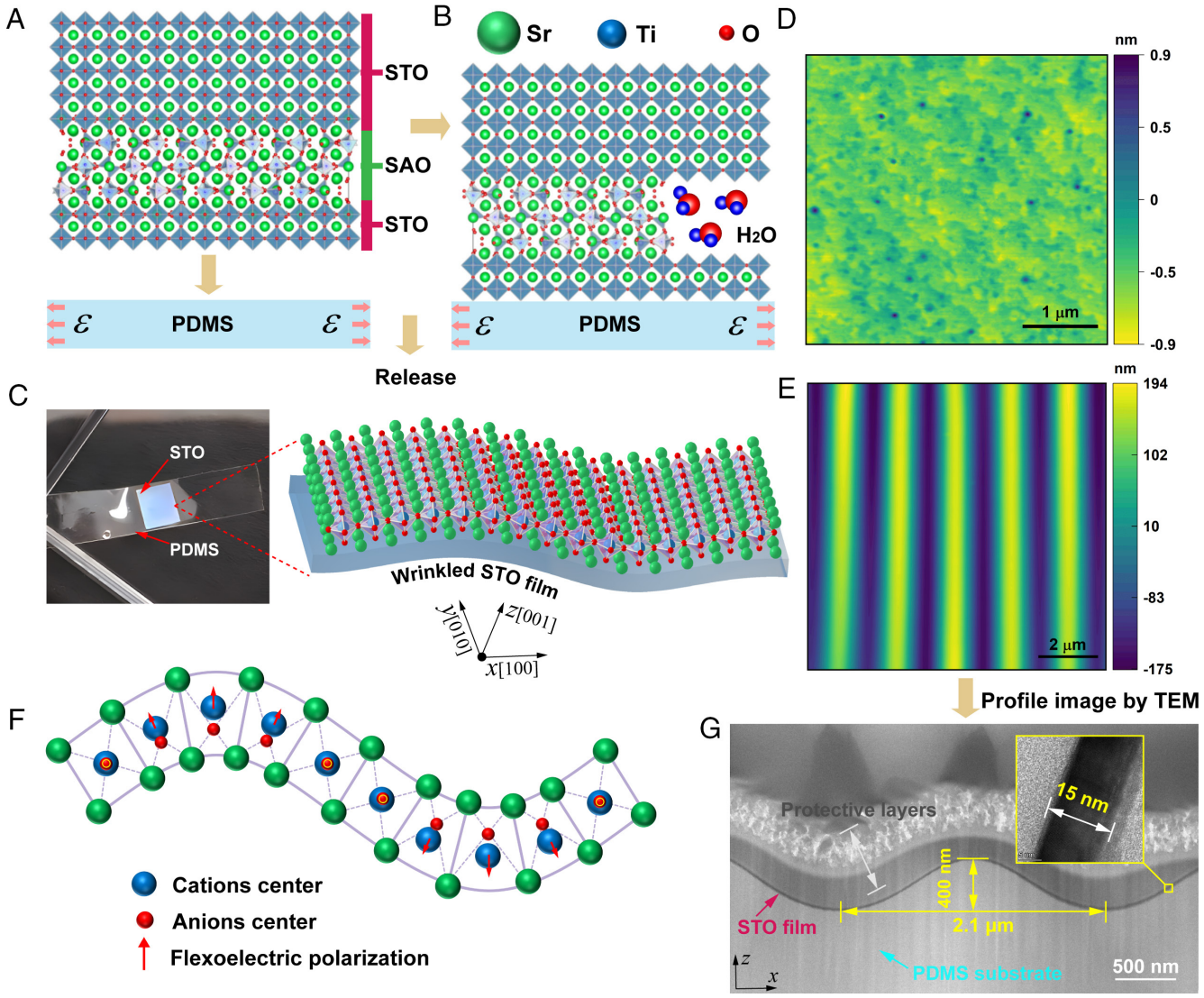

Fig. 1. Fabrication and characterizations of wrinkled STO films. (*A*) The STO/SAO/STO multilayer synthesized with a pulsed laser deposition (PLD) system is attached to a pre-stretched PDMS substrate. (*B*) The SAO layer is dissolved in deionized water. (*C*) The STO nanofilm (5 mm × 5 mm) is transferred onto the PDMS substrate and forms wrinkled microcosmic morphology by releasing the pre-strain. (*D* and *E*) The flat and the striped STO morphologies without and with pre-strains, respectively, are probed by AFM scanning. (*F*) Schematic diagram of charge center shifts owing to wrinkle-induced strain gradients, indicating flexoelectric polarizations in unit cells. (*G*) Low-magnification STEM image of two whole crest–valley wrinkles. The film thickness is measured to be 15 nm. Here, the PDMS/STO system is subjected to a pre-strain of 10%, the wrinkle wavelength is $\lambda \approx 2.1$ μm and the amplitude is $A \approx 200$ nm.

(*SI Appendix*, Fig. S1) of the flat STO films transferred without pre-strain using the atomic force microscope (AFM) and high-resolution X-ray diffraction (HRXRD) characterizations (*Materials and Methods*), indicating the high-quality surface and good single-crystalline of the STO films. For the case with a uniaxial pre-strain of 10%, we obtained ordered striped STO wrinkles with a 400 nm peak-to-peak amplitude and a 2.1 μm wavelength (Fig. 1*E*), which is consistent with the value measured by scanning transmission electron microscopy (STEM) (Fig. 1*G*). Benefiting from such spontaneous surface wrinkling, we can conveniently achieve large-area, self-assembled, and continuously tunable strain gradients in the STO film. The strain gradients can break the local symmetry and shift the charge centers within the centrosymmetric STO lattices, thereby resulting in flexoelectric polarizations at the crests and valleys of the wrinkled STO nanofilms (Fig. 1*F*).

Observation of the Polar Patterns. To examine the polar state of the wrinkled STO films, we conducted PFM measurements at the wrinkled STO surface, as shown in Fig. 2. The PFM measurements (*Materials and Methods*) were executed using a conductive PtIr-coated tip under the Dual Alternating Current (AC) Resonance-Tracking (DART) mode, with the bottom surface grounded (Fig. 2*A*). For comparison, we also measured the PFM amplitude and phase of a flat STO film before the transfer (*SI Appendix*, Fig. S2), indicating no organized polar structures in paraelectric STO film at room temperature. From Fig. 2 *E*–*G*, it was found that the measured PFM amplitude (Fig. 2*F*) and phase (Fig. 2*G*) responses were dramatically enhanced at the valleys and crests of the wrinkles compared to those of flat STO film (*SI Appendix*, Fig. S2). These results indicated the formation of a striped polar pattern (Fig. 2 *C* and *D*) in the STO film owing to the wrinkling deformation. Here, the polar state in wrinkled STO films is determined by various electromechanical coupling effects (5), among which the coupling between strain gradients and polarization (flexoelectricity) plays the dominant role. This is because the strain gradients are dramatically enhanced (up to $10^{6\sim7}$ m^{-1}) by reducing the film thickness to the nanometer scale, while the piezoelectricity and ferroelectricity are both negligible due to the centrosymmetry of the room-temperature STO (22, 36).

Furthermore, we have conducted a theoretical analysis (see details in *SI Appendix*, *Supplementary Note* 1) to understand the macroscopic mechanism of the polar stripe in the wrinkled STO nanofilms. From the observed periodic striped morphology, the analytical solution of the wrinkle deflection can be described as a cosine wave $w = A\cos(2\pi x/\lambda)$ (29, 37) for simplicity. w is the wrinkle deflection, A is the wrinkle amplitude, and λ is the wavelength, see *SI Appendix*, Eq. **S9** for details. The wrinkle-induced strain gradient $\varepsilon_{xx,z}$ can be approximately described by the local curvature of the wrinkle morphology as a function of the wrinkle amplitude and wavelength,

$$\varepsilon_{xx,z} = \frac{4\pi^2 A}{\lambda^2}\cos\left(\frac{2\pi x}{\lambda}\right), \quad [1]$$

where

$$A = h\sqrt{(1+\eta^2)\left(\frac{\varepsilon_{11}^0}{\varepsilon_c}-1\right)},\ \lambda = 2\pi h\left[\frac{(1+\eta^2)\overline{E}_f}{3\overline{E}_s}\right]^{\frac{1}{3}}, \quad [2]$$

and h is the film thickness, $\overline{E}_s = E_s/(1-v_s^2)$, $\overline{E}_f = E_f/(1-v_f^2)$, E and v denote the Young's modulus and the Poisson's ratio, respectively. The subscripts s, and f refer to the substrate and film, respectively. η is an electromechanical coupling coefficient caused by the size-dependent flexoelectricity (*SI Appendix*, *Supplementary Note* 1). ε_{11}^0 is the pre-stretched strain and ε_c (*SI Appendix*, Eq. **S10**) is the critical strain of wrinkling. Then the flexoelectric polarization can be given by:

$$P_z = P_0\cos\left(\frac{2\pi x}{\lambda}\right), \quad [3]$$

where the peak polarization P_0 is

$$P_0 = \frac{4\pi^2 A u_{13}}{\lambda^2}. \quad [4]$$

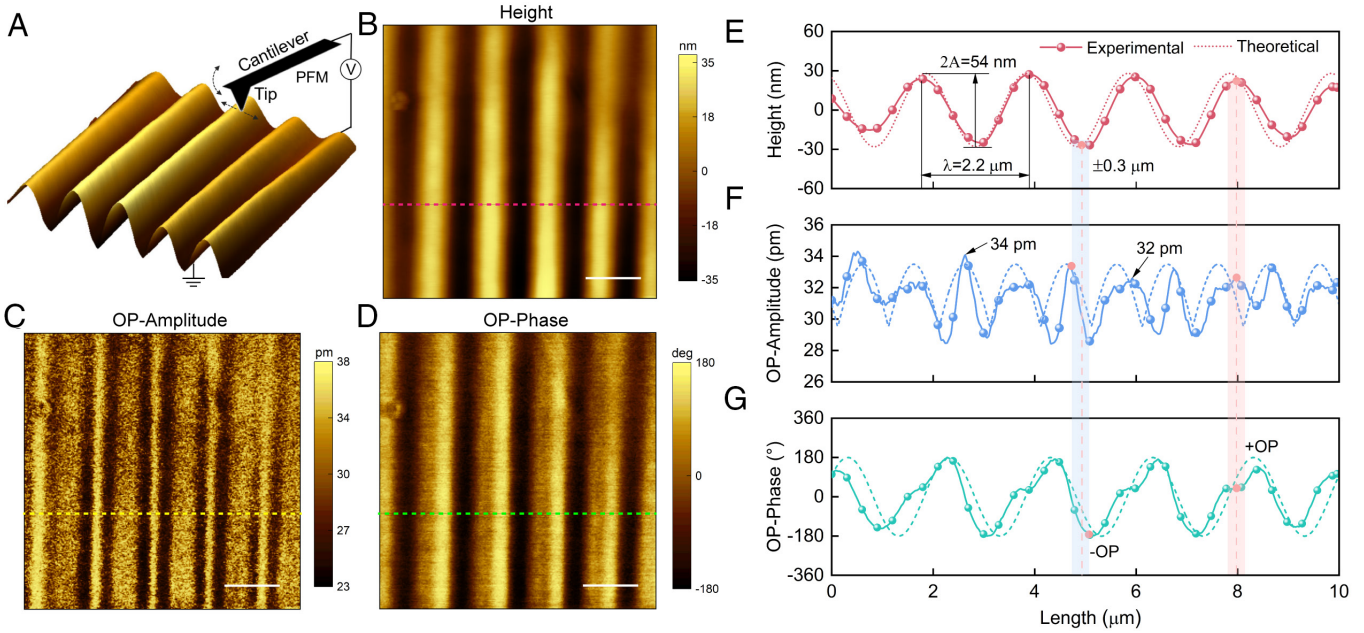

Fig. 2. The PFM responses of stripe-wrinkled STO film. (*A*) The three-dimensional (3D) morphology of wrinkled STO film and the schematic diagram of PFM scanning. (*B*) The striped wrinkle pattern. The out-of-plane (OP-) PFM amplitude (*C*) and phase (*D*) responses. (*E*–*G*) The curves of profile values along, red, yellow, and green dashed lines in panels *B*–*D*, respectively. Film thickness: 15 nm; (Scale bars: 2 μm.)

Using the material constants discussed in *SI Appendix, Supplementary Note* 1, we can theoretically calculate the periodic wrinkle morphology and corresponding flexoelectric polarization distribution, which agree well with our PFM measurements, as shown in Fig. 2 *E*–*G*. According to our theoretical analysis, it is the opposite strain gradients (local curvatures) at the wrinkle crests and valleys that are macroscopically responsible for the periodic polar patterns, as shown in Fig. 2 *F* and *G*. It should be noticed that the measured PFM amplitude responses (Fig. 2*F*) are both enhanced at the wrinkle crests and valleys owing to the AC component of the PFM drive voltage. However, it is challenging to quantitatively analyze the magnitude of the flexoelectric polarization using the current PFM results. We can only qualitatively conclude that periodic polar structures are produced in the wrinkled STO film. Further verification through atomistic simulations and quantitative experiments is needed to fully understand these wrinkle-induced flexoelectric polar patterns. Moreover, it should be noticed that the measured PFM OP-Amplitudes are asymmetric (Fig. 2*F*) at the crests and valleys, while the theoretical predictions should be symmetric. We attribute this anomalous discrepancy to the strong interplay between the sharp PFM tip and the wrinkle morphology since the DART PFM operates in a contact mode. In this mode, sharp tip-induced strain gradients (18, 38), and the electrostatic interactions (39) are inevitable.

To exclude the complex interference caused by the tip contact, we have probed the surface potential of the flat (*SI Appendix*, Fig. S3) and wrinkled (*SI Appendix*, Fig. S4) STO films using a noncontact Scanning Kelvin Probe Force Microscopy (SKPM) mode. When the STO film is polarized by wrinkle-induced flexoelectricity, a corresponding flexoelectric field is constructed inside the film, as demonstrated in our SKPM experiments by measuring the upper surface potential with the bottom surface grounded (*SI Appendix*, Fig. S4*C*). Compared to the trivial surface potential of the flat STO film (*SI Appendix*, Fig. S3*B*), the surface potential in wrinkled STO film demonstrates a periodic enhancement and striped pattern (*SI Appendix*, Fig. S4*E*) that corresponds to the wrinkle morphology (*SI Appendix*, Fig. S4 *A* and *D*). Similar to the PFM results, the different strain gradients and corresponding flexoelectricity at the crests and valleys account for such a periodic surface potential (*SI Appendix*, Fig. S4*B*).

Mechanical Manipulation. The nature of the wrinkling phenomenon is the surface instability caused by the compressive strain. In the absence of other stimuli, the compressive strain exerted on the STO/PDMS system is numerically equal to the pre-stretched strain initially imposed on the PDMS substrate. However, when subjected to an extra stretching strain $\varepsilon_{applied}$, as shown in Fig. 3*A*, the wrinkled system will reach a new equilibrium state. Then the effective compressive strain imposed on the system is $\varepsilon_{eff} = \varepsilon_{pre} - \varepsilon_{applied}$, and the effective wrinkle amplitude and wavelength approximately become (27)

$$A_{eff} = h\sqrt{\left(1+\eta^2\right)\left(\frac{\varepsilon_{eff}}{\varepsilon_c}-1\right)},$$
$$\lambda_{eff} = 2\pi h\left[\frac{\left(1+\eta^2\right)\overline{E}_f}{3\overline{E}_s}\right]^{\frac{1}{3}}\left(1+\varepsilon_{applied}\right). \quad [5]$$

As a result, the wrinkle-induced strain gradients in Eq. **1** and corresponding polarization in Eq. **4** can be mediately manipulated by the applied stretching strain $\varepsilon_{applied}$ With an initial pre-strain of 10%, we obtained a striped wrinkle with a 400 nm peak-to-peak height and a 2.1 μm wavelength (Fig. 1*G*). By varying applied stretching strain (*Materials and Methods*), both the wrinkle amplitude and wavelength were changed, as shown in Fig. 3*B*. The wrinkle amplitude (A) dramatically decreases from 200 nm to 27 nm by increasing the applied stretching strain to about 9.7%, while the wrinkle wavelength (λ) slightly increases from 2.1 μm to 2.2 μm, which is consistent with our theoretical analysis (Fig. 3*B*). Correspondingly, the trend of the PFM OP-amplitude (Fig. 3 *D* and *F*) is similar to that of the wrinkle morphology, which is attributed to various wrinkle-induced strain gradients (Fig. 3*E*). The experimental strain gradient values in Fig. 3*E* are obtained by performing curvature analysis (1) at the peaks of various wrinkle morphologies measured by AFM, while the theoretical values are calculated by Eq. **1**. The error bars in Fig. 3 *E* and *F* are estimated using the measured data of five waves in a 10 × 10 μm^2 area.

Atomic-Scale Polar Structure. To elucidate the atomic polar structure inside the wrinkled STO film, we acquired the atomic resolution images (Fig. 4) of the film cross-section using the aberration-corrected HAADF Z-contrast STEM imaging (*Materials and Methods*). A sectional slice of two whole valleys and one crest was prepared (*SI Appendix*, Fig. S5) by a focus ion beam (FIB) (*Materials and Methods*). The element composition and the atomic fractions of the STO films were further identified by surface scanning with an Energy Dispersive Spectrometer (EDS), as shown in *SI Appendix*, Fig. S6. Then the lattice structures of the valley (Fig. 4*c*1) and crest (Fig. 4*d*1) were visualized by conducting HAADF-STEM scanning at the selected regions (red box in Fig. 4*A* and green box in Fig. 4*B*). The flat strain-free STO is nonpolar with a symmetric cubic structure (*SI Appendix*, Fig. S7*A*), whereas the symmetry will be broken by the wrinkle-induced inhomogeneous strains (strain gradients). Then both the oxygen octahedra and the Ti^{4+} are displaced from the center of the Sr^{2+} tetragonal cell in wrinkled STO, resulting in a local polarization (*SI Appendix*, Fig. S7*B*). The Ti^{4+} displacement vectors and corresponding polarizations can be determined by performing a two-dimensional (2D) Gaussian peak fitting (3, 7, 40) on the atomic resolution images. Therefore, we were able to map the displacement vectors of Ti^{4+} ($\delta_{Ti\text{-}Sr}$) at the valley and crest, respectively, as shown in Fig. 4 c2 and d2. The Ti^{4+} displacement vectors denoted by the yellow arrows coincide with the corresponding polarization directions in the unit cells (40), which was further verified by our first-principles calculations (*SI Appendix*, Figs. S10). Using the linear relationship between the polarization and the Ti^{4+} displacement ($P \propto \delta_{Ti-Sr}$ μC cm^{-2}) (*Materials and Methods*), we calculated the magnitude of the polarizations, as shown in *SI Appendix*, Fig. S8. We found that the polarization directions were predominantly downward with an average magnitude of about 38 μC cm^{-2} at the valley, whereas they were predominantly upward with an average magnitude of about 45 μC cm^{-2} at the crest. It is this specific polarization distribution, with opposite directions at the valleys and crests, that gives rise to the periodic polar pattern observed in our PFM tests.

To examine the roles of strains and strain gradients in the polar structures, we mapped the in-plane (ε_{xx}) and out-of-plane (OP) (ε_{zz}) strain fields using geometrical phase analysis (GPA) (41, 42) of the atomic resolution images. Apparent strain gradients along the OP direction ($\varepsilon_{xx,z}$) were observed in the in-plane strain fields of both the valley (Fig. 4*E*) and crest (Fig. 4*F*), whereas no significant strain gradients could be found in the OP strain fields

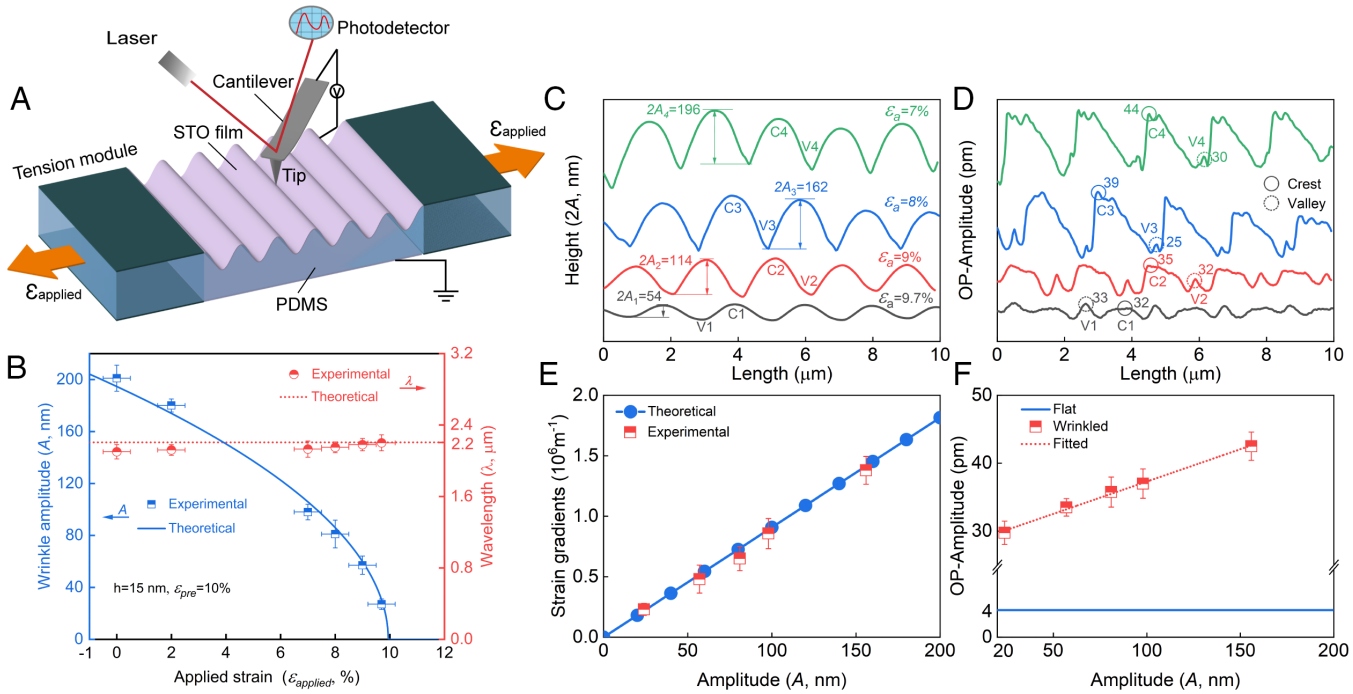

Fig. 3. The tunability of wrinkle-induced strain gradients and corresponding PFM responses. (*A*) A schematic diagram of the PFM test with an applied tensile strain $\varepsilon_{applied}$ to the wrinkled STO/PDMS system. (*B*) The wrinkle amplitude (blue) and wavelength (red), as a function of the applied strain, indicate that the wrinkle morphology can be manipulated by the applied strain. The initial pre-strain here is $\varepsilon_{11}^{0} = 10\%$. The error bars are the SD, and the primary error stems from the tension module and the slight biases of scanning area in different PFM tests. (*C* and *D*) Measured wrinkle amplitudes (*C*) and corresponding vertical PFM responses (*D*) upon varying applied tensile strains. The letters "V" and "C" denote the valley (dashed circle) and crest (solid circle) regions, respectively. (*E* and *F*) The magnitudes of (*E*) strain gradients and the (*F*) vertical PFM response, as a function of wrinkle amplitude, indicating the wrinkle-induced strain gradients and corresponding electric polarization can be tunned by wrinkle morphology. The error bars in *E* and *F* represent the SD.

(*SI Appendix*, Fig. S9). The profile values of the selected yellow dash lines in Fig. 4 *E* and *F* were plotted in Fig. 4*G*, where the slopes of the fitted curves represent the corresponding strain gradients. It is found that the directions of the strain gradients ($\varepsilon_{xx,z}$) were coincident with the displacements of Ti^{4+} and corresponding polarizations. Quantitatively, the magnitudes of the strain gradients at the valley and crest are about 4×10^6 m^{-1}, which is consistent with our theoretical prediction and AFM measurements (about 2×10^6 m^{-1} in Fig. 3*E*). The inevitable cross-scale factors that exist between microscopic and macroscopic analyses may account for this acceptable discrepancy.

It is worth emphasizing that perceptible ferroelectricity or piezoelectricity occurs when the symmetry of the STO crystal is broken by strain gradients. As a result, the local polar structures will be determined by the delicate competition between the strains and strain gradients. Considering the ferroelectricity or piezoelectricity in the wrinkled STO film, the tensile regions tend to present in-plane polarization orientations, while the compressive regions prefer OP ones, as demonstrated in bent ferroelectric films (43, 44). According to the results in Fig. 4*G*, we found that the wrinkled STO film was subjected to more tensile strain than the pure bending case, where the tensile and compressive strains on both sides of the film should be anti-symmetric. Two main factors might account for this phenomenon. On one hand, the neutral surface ($\varepsilon_{zz} = 0$) of the film at the valley and crest regions was shifted from the center of the film section due to the constraining effect of the substrate. On the other hand, the whole film was stretched to adapt to the large deformation of the compliant substrate. Influenced by such a tensile strain field, the polarization directions in Fig. 4 *c*2 and *d*2 exhibit local in-plane components owing to the strain-induced dipole rotations (43, 44). However, the polarizations probed at both the valley and crest were predominantly OP, indicating that the strain gradients associated with flexoelectricity played the dominant role in forming the polar structures of the current wrinkled STO film.

To further understand the origin of the wrinkle-induced flexoelectric polar structures observed in our experiments, we conducted first-principles density functional theory (DFT) calculations (see details in *Materials and Methods*). After the structure optimization, the wrinkling deformation and corresponding strain gradients are imposed on the STO film (*SI Appendix*, Fig. S10*A*). To verify the directions of the displacements of Ti atoms, we calculated the electron density difference between the wrinkled STO film and the corresponding Sr, Ti, and O atoms, as shown in *SI Appendix*, Fig. S10*B*. The increased electron density between the Ti atoms and the top and bottom O atoms indicates the Ti atoms are displaced toward the top surface at the crest while toward the bottom surface at the valley, as illustrated in *SI Appendix*, Fig. S10*B*, which is consistent with our experimental findings (Fig. 4 *c*2 and *d*2). Then we directly calculated the local polarization in each unit cell by utilizing the Born effective charges and the atomic displacements relative to the cubic phase of all atoms, as shown in Fig. 4*h*. The results indicate that both local polarizations and Ti atom displacements show a periodic sinusoidal waveform trend, which is upward at the crest and downward at the valley. Correspondingly, the direction of the flexoelectric electric field generated at the crest is downward, and the one at the valley is upward, which is consistent with the surface potential measured by SKPM (*SI Appendix*, Fig. S4). Moreover, we calculated the Bader charges of all atoms in the wrinkled STO. At the crest, we find that the resultant Bader charge on the bottom Sr-O-Sr surface of each unit cell is larger than that on the top surface (Fig. 4*I*), indicating a downward shift of the negative charge center as well

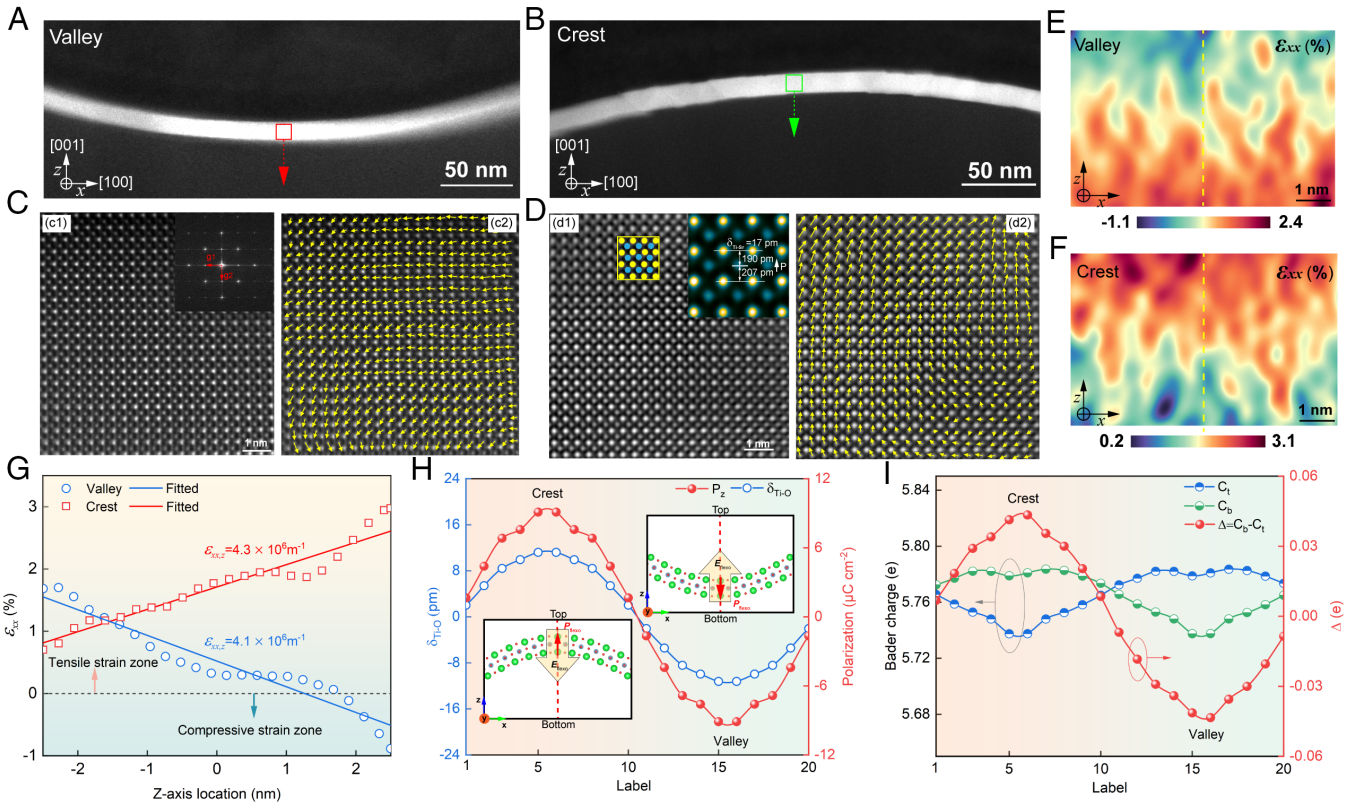

Fig. 4. Atomic-scale analysis of the wrinkle-induced polar structure. (*A* and *B*) Low-magnification STEM images of the (*A*) valley and (*B*) crest sections of the wrinkled STO film. (*C* and *D*) HAADF-STEM images and Ti^{4+} displacement vectors. (*c*1 and *d*1) The atomically resolved HAADF-STEM images from the red and green squares in panels *A* and *B*, respectively. The *Inset* in *c*1 shows the FFT pattern of *c*1 with the reciprocal lattice vectors g1 and g2, which are used in GPA analysis. The *Top-Right Inset* in *d*1 shows the magnified image of the yellow box in *d*1, indicating a typical distorted lattice. (*c*2 and *d*2) Atomic Ti^{4+} displacement vectors (δ_{Ti-Sr}, denoted by red arrows) overlaid on the HAADF-STEM images, indicating predominantly (*c*2) downward and (*d*2) upward polarization fields at the valley and crest, respectively. (*E* and *F*) Maps of the in-plane strain fields obtained from GPA, indicating apparent OP strain gradients. (*G*) Line profiles of the corresponding strain values along the yellow dotted lines in *E* and *F*, indicating more tensile strains than the compressive ones in the wrinkled STO films. The strain gradients were calculated by the curve slops. (*H*) The Ti displacements away from the center of the oxygen octahedron and the corresponding polarization calculated by DFT. (*I*) The Bader charge distribution calculated by DFT. C_t and C_b represent the resultant Bader charge on the top and bottom Sr-O-Sr surface of each unit cell, respectively.

as an upward flexoelectric polarization field. Using the same methodology, we find a downward flexoelectric polarization field at the valley, which agrees well with our experimental results.

Conclusions

In summary, we report the realization and manipulation of the ordered periodic polar patterns in the wrinkled nonpolar STO nanofilms at room temperature. We demonstrate that the pronounced polarization (up to 40 μC cm^{-2}) at the valleys and crests is primarily attributed to the huge wrinkle-induced strain gradient, which can be manipulated by tuning the imposed strain boundary conditions on the wrinkled film/substrate system. At the atomic scale, our results of atomic resolution imaging and first-principles calculations further reveal that the wrinkle-induced polarization vectors are determined by both local strain and strain gradients. Particularly, the wrinkle-induced tensile strains lead to in-plane dipole rotations, whereas the overall polarizations are predominantly OP oriented since the OP strain gradients associated with flexoelectricity play a dominant role in such wrinkled nonpolar STO nanofilms. Not limited to STO nanofilms, the reported wrinkle-induced ordered polar patterns are generic and can be applied to other polar and nonpolar dielectrics, where flexoelectricity generally works. Additionally, this study can also serve as a general platform for exploring strain gradient engineering and flexoelectric domain engineering, which are crucial for future nanoelectronics.

Materials and Methods

Fabrication of Wrinkled STO Films. A sacrificial layer of SAO with a thickness of 10 nm was initially epitaxially grown onto a (001)-oriented STO substrate using a PLD system with a 248 nm wavelength KrF excimer laser at 750 °C under an oxygen pressure of 1×10^{-2} Pa. Subsequently, a 15 nm STO layer was epitaxially grown at 720 °C under an oxygen pressure of 15 Pa. The target-substrate distance was 9 cm, and the laser energy was approximately 250 mJ with a laser pulse rate of 5 Hz. Finally, the STO/SAO/STO epitaxial heterostructure was gradually cooled down to room temperature at a rate of 10 °C/min. The STO/SAO/STO heterostructure was adhered to a pre-stretched PDMS substrate and immersed in deionized water until the SAO layer was fully dissolved. After evaporating the residual water and releasing the pre-strain, the STO film was spontaneously wrinkled along with the shrinkage of the PDMS substrate.

Crystal Structure Characterization. The crystal structures were characterized by a high-resolution X-ray diffractometer (HRXRD) using a SmartLab3KW instrument. The incident X-ray was generated from a Cu $K\alpha_1$ source.

PFM. PFM measurements were carried out by a commercial AFM (Oxford Instruments) system in DART mode under ambient conditions. The PFM responses and morphologies were measured by a Pt/Ir-coating conductive probe (PPP-EFM-50, Nanosensors) with a tip height of 15 μm, a tip curvature radius of about 25 nm, a resonance frequency of 75 kHz, and a force constant of 2.8 N m^{-1}. For the non-contact SKPM mode, the distance between the probe and the sample surface was set to 50 nm.

Stretching Experiment. The stretching PFM experiments were conducted by the same AFM system (Oxford Instruments) system equipped with a customized stretching platform (NanoRack). The applied tensile strains were monitored by several displacement sensors installed on the platform.

STEM. Aberration-corrected HAADF Z-contrast STEM was performed on a (scanning) transmission electron microscope (FEI Titan Themis 300 kV) that combines outstanding high-resolution STEM and TEM imaging with industry-leading EDS signal detection. 2D/3D chemical characterization with compositional mapping was performed by four in-column silicon drift detector Super-X detectors with unique cleanliness. The STEM samples were prepared using a FIB by cutting the wrinkled STO film along the thickness direction. Before cutting, C-protection layers with greater stiffness than the PDMS substrate were deposited to prevent sample damage and stress relaxation during the ion milling. The voltage of the ion thinning process was gradually reduced.

Estimation of the Polarization Caused by B-Site Cation. To quantitatively calculate the polarization in each lattice cell, we need to obtain the exact position information of Sr, Ti, and O atoms from the high-resolution HAADF-STEM images. However, it is challenging to explicitly obtain the O atom displacements due to the lack of contrast in HAADF-STEM imaging. As an alternative approach, we used the displacement vector of Ti^{4+} (symbolized by $\delta_{Ti\text{-}Sr}$ in *SI Appendix*, Fig. S7*B*) relative to the center of its four corners neighboring Sr^{2+} to estimate the polarizations in unit cells. This approach (45) is based on a simple empirical linear relationship between the local polarization (P) and the displacement of cations ($\delta_{Ti\text{-}Sr}$): ($P \propto \delta_{Ti-Sr}\ \mu C\,cm^{-2}$) and has been demonstrated to effectively evaluate the displacive polarization in STO (40, 46, 47).

First-Principles DFT Calculations. Following our experimental setup, we constructed a slab STO model (1 × 20 × 1 cells) and imposed a sinusoidal deflection to the system. The calculations were performed by using the Vienna ab initio simulation package based on density function theory (48, 49), within the local density approximation. The electron-ionic core interaction was treated by a projector augmented wave potential that explicitly includes the valence electrons of 4 s, 4p, 5 s for Sr, 3 s, 3p, 3d, 4 s for Ti, and 2 s, 2p for O. The self-consistent loops of calculations were iterated until the condition of convergence was satisfied. The total energy difference between two adjacent iterating steps was less than 1×10^{-6} eV. The electronic wave functions were expanded in plane waves up to a cut-off energy of 500 eV. The conjugate-gradient algorithm was used in this computational scheme to relax the ions until the force on each atom is less than 0.005 eV/Å. We performed *k*-point convergence studies by use of a uniform Monkhorst-Pack scheme. The *k*-point sampling was set to a 1 × 6 × 1 mesh for the STO structures. The obtained lattice parameter for STO is 3.871 Å and c/a = 1.00001. The polarization was then calculated using the Born effective charges (*SI Appendix*, *Supplementary Note 2*).

Data, Materials, and Software Availability. All data, materials, and experimental procedures that support the findings in this study are available in the main text, *Materials and Methods*, and/or *SI Appendix*.

ACKNOWLEDGMENTS. This study was supported by the National Natural Science Foundation of China (No. 12122209, 12072251, 12472157), and Project B18040.

Author affiliations: [a]State Key Laboratory for Strength and Vibration of Mechanical Structures, School of Aerospace Engineering, Xi'an Jiaotong University, Xi'an 710049, China; and [b]School of Mechanical Engineering and Automation, Fuzhou University, Fuzhou 350108, China

1. C. Chen *et al.*, Large-scale domain engineering in two-dimensional ferroelectric CuInP2S6 via giant flexoelectric effect. *Nano Lett.* **22**, 3275–3282 (2022).
2. Y. Nahas *et al.*, Inverse transition of labyrinthine domain patterns in ferroelectric thin films. *Nature* **577**, 47–51 (2020).
3. Y. J. Wang *et al.*, Polar meron lattice in strained oxide ferroelectrics. *Nat. Mater.* **19**, 881–886 (2020).
4. S. Das *et al.*, Observation of room-temperature polar skyrmions. *Nature* **568**, 368–372 (2019).
5. L. Han *et al.*, High-density switchable skyrmion-like polar nanodomains integrated on silicon. *Nature* **603**, 63–67 (2022).
6. Y. T. Shao *et al.*, Emergent chirality in a polar meron to skyrmion phase transition. *Nat. Commun.* **14**, 1355 (2023).
7. A. K. Yadav *et al.*, Observation of polar vortices in oxide superlattices. *Nature* **530**, 198–201 (2016).
8. C. Tan *et al.*, Engineering polar vortex from topologically trivial domain architecture. *Nat. Commun.* **12**, 4620 (2021).
9. M. R. M. Shang-Lin Hsu *et al.*, Emergence of the Vortex State in Confined Ferroelectric Heterostructures. *Adv. Mater.* **31**, 1901014 (2019).
10. Y. Tang *et al.*, Observation of a periodic array of flux-closure quadrants in strained ferroelectric PbTiO3 films. *Science* **348**, 547–551 (2015).
11. G. Catalan *et al.*, Flexoelectric rotation of polarization in ferroelectric thin films. *Nat. Mater* **10**, 963–967 (2011).
12. A. Y. Abid *et al.*, Creating polar antivortex in PbTiO(3)/SrTiO(3) superlattice. *Nat. Commun.* **12**, 2054 (2021).
13. D. A. Tenne *et al.*, Ferroelectricity in ultrathin BaTiO3 films: Probing the size effect by ultraviolet Raman spectroscopy. *Phys. Rev. Lett.* **103**, 177601 (2009).
14. D. J. Kim *et al.*, Polarization relaxation induced by a depolarization field in ultrathin ferroelectric BaTiO3 capacitors. *Phys. Rev. Lett.* **95**, 237602 (2005).
15. T. D. Nguyen, S. Mao, Y. W. Yeh, P. K. Purohit, M. C. Mcalpine, Nanoscale flexoelectricity. *Adv. Mater.* **25**, 946–974 (2013).
16. P. Zubko *et al.*, Flexoelectric effect in solids. *Annu. Rev. Mater. Res.* **43**, 387–421 (2013).
17. P. V. Yudin, A. K. Tagantsev, Fundamentals of flexoelectricity in solids. *Nanotechnology* **24**, 432001 (2013).
18. S. Das *et al.*, Enhanced flexoelectricity at reduced dimensions revealed by mechanically tunable quantum tunnelling. *Nat. Commun.* **10**, 1–7 (2019).
19. M. S. Majdoub, P. Sharma, T. Cagin, Enhanced size-dependent piezoelectricity and elasticity in nanostructures due to the flexoelectric effect. *Phys. Rev. B* **77**, 125424 (2008).
20. D. Lee *et al.*, Giant flexoelectric effect in ferroelectric epitaxial thin films. *Phys. Rev. Lett.* **107**, 057602 (2011).
21. W. Ming *et al.*, Flexoelectric engineering of van der Waals ferroelectric CuInP2S6. *Sci. Adv.* **8**, eabq1232 (2022).
22. S. Cai *et al.*, Enhanced polarization and abnormal flexural deformation in bent freestanding perovskite oxides. *Nat. Commun.* **13**, 1–10 (2022).
23. H. Shang, X. Liang, F. Deng, S. Hu, S. Shen, Flexoelectricity in wrinkled thin films. *Int. J. Mech. Sci.* **234**, 107685 (2022).
24. H. Yamahara *et al.*, Flexoelectric nanodomains in rare-earth iron garnet thin films under strain gradient. *Commun. Mater.* **2**, 1–8 (2021).
25. P. Zubko, G. Catalan, A. Buckley, P. Welche, J. F. Scott, Strain gradient induced polarization in SrTiO3 single crystals. *Phys. Rev. Lett.* **99**, 167601 (2007).
26. L. Wang *et al.*, Flexoelectronics of centrosymmetric semiconductors. *Nat. Nanotechnol.* **15**, 661–667 (2020).
27. H. Jiang *et al.*, Finite deformation mechanics in buckled thin films. *Proc. Natl. Acad. Sci. U.S.A.* **104**, 15607–15612 (2007).
28. N. Bowden, S. Brittain, A. G. Evans, J. W. Hutchinson, G. M. Whitesides, Spontaneous formation of ordered structures in thin films of metals supported on an elastomeric polymer. *Nature* **393**, 146–149 (1998).
29. Z. Y. Huang, W. Hong, Z. Suo, Nonlinear analyses of wrinkles in a film bonded to a compliant substrate. *J. Mech. Phys. Solids* **53**, 2101–2118 (2005).
30. L. Zhou *et al.*, Dynamic interpenetrating polymer network (IPN) strategy for multiresponsive hierarchical pattern of reversible wrinkle. *ACS Appl. Mater Interfaces* **11**, 15977–15985 (2019).
31. T. Xu *et al.*, Mechanical rippling for diverse ferroelectric topologies in otherwise nonferroelectric SrTiO3 nanofilms. *Phys. Rev. Lett.* **132**, 086801 (2024).
32. H. Shang *et al.*, Mechanical control of polar patterns in wrinkled thin films via flexoelectricity. *Phys. Rev. Lett.* **132**, 116201 (2024).
33. H. Jiang *et al.*, Finite deformation mechanics in buckled thin films on compliant supports. *Proc. Natl. Acad. Sci. U.S.A.* **104**, 15607–15612 (2007).
34. P. Salles *et al.*, On the role of the Sr3−xCaxAl2O6 sacrificial layer composition in epitaxial La0.7Sr0.3MnO3 membranes. *Adv. Funct. Mater.* **33**, 2304059 (2023).
35. K. Gu *et al.*, Simple method to obtain large-size single-crystalline oxide sheets. *Adv. Funct. Mater.* **30**, 2001236 (2020).
36. P. Zubko, G. Catalan, A. Buckley, P. R. Welche, J. F. Scott, Strain-gradient-induced polarization in SrTiO3 single crystals. *Phys. Rev. Lett.* **99**, 167601 (2007).
37. F. Brau *et al.*, Multiple-length-scale elastic instability mimics parametric resonance of nonlinear oscillators. *Nat. Phys.* **7**, 56–60 (2010).
38. H. Lu, C. W. Bark, D. Ojos, J. Alcala, A. Gruverman, Mechanical writing of ferroelectric polarization. *Science* **336**, 59–61 (2012).
39. X. Liang, Y. Yu, R. Liu, W. Liu, S. Shen, Flexoelectricity in periodically poled lithium niobate by PFM. *J. Phys. D Appl. Phys.* **55**, 335303 (2022).
40. D. Lee *et al.*, Emergence of room-temperature ferroelectricity at reduced dimensions. *Science* **349**, 1314–1317 (2015).
41. M. Hÿtch, E. Snoeck, R. Kilaas, Quantitative measurement of displacement and strain fields from HREM micrographs. *Ultramicroscopy* **74**, 131–146 (1998).
42. J. L. Rouviere, E. Sarigiannidou, Theoretical discussions on the geometrical phase analysis. *Ultramicroscopy* **106**, 1–17 (2005).
43. G. Dong *et al.*, Periodic wrinkle-patterned single-crystalline ferroelectric oxide membranes with enhanced piezoelectricity. *Adv. Mater* **32**, 2004477 (2020).
44. G. Dong *et al.*, Super-elastic ferroelectric single-crystal membrane with continuous electric dipole rotation. *Science* **366**, 475–479 (2019).
45. S. C. Abrahams, S. K. Kurtz, P. B. Jamieson, Atomic displacement relationship to curie temperature and spontaneous polarization in displacive ferroelectrics. *Phys. Rev.* **172**, 551–553 (1968).
46. P. Gao *et al.*, Atomic-scale measurement of flexoelectric polarization at SrTiO_3 dislocations. *Phys. Rev. Lett.* **120**, 267601 (2018).
47. C. Song *et al.*, Electronic origin of laser-induced ferroelectricity in SrTiO(3). *J. Phys. Chem. Lett.* **14**, 576–583 (2023).
48. G. Kresse, J. Furthmüller, Efficient iterative schemes for ab initio total-energy calculations using a plane-wave basis set. *Phys. Rev. B* **54**, 11169 (1996).
49. P. E. Blöchl, Projector augmented-wave method. *Phys. Rev. B* **50**, 17953 (1994).